AIAA JOURNAL
Vol. 47, No. 8, August 2009

Large-Eddy Simulations of a Supersonic Jet and Its Near-Field Acoustic Properties

Junhui Liu,* K. Kailasanath,† and Ravi Ramamurti‡
Naval Research Laboratory, Washington, D.C. 20375
David Munday§ and Ephraim Gutmark¶
University of Cincinnati, Cincinnati, Ohio 45221-0070
and
Rainald Lohner**
George Mason University, Fairfax, Virginia 22030

DOI: 10.2514/1.43281

Large-eddy simulations of imperfectly expanded jet flows from a convergent–divergent nozzle with a sharp contraction at the nozzle throat have been carried out. The flowfield and near-field acoustics for various total pressure ratios from overexpanded to underexpanded jet flow conditions have been investigated. The location and spacing of the shock cells are in good agreement with experimental data and previous theoretical results. The velocity profiles are also in good agreement with data from experimental measurements. A Mach disk is observed immediately downstream of the nozzle exit for overexpanded jet conditions with nozzle pressure ratios much lower than the fully expanded value. It is found that this type of nozzle with a sharp turning throat does not have a shock-free condition for supersonic jet flows. The near-field intensities of pressure fluctuations show wavy structures for cases in which screech tones are observed. The large-eddy simulations predictions of the near-field noise intensities show good agreement with those obtained from experimental measurements. This good agreement shows that large-eddy simulations and measurements can play complementary roles in the investigation of the noise generation from supersonic jet flows.

Nomenclature

D	=	nozzle exit diameter
D_j	=	fully expanded jet diameter
L_s	=	shock-cell spacing
M_j	=	fully expanded jet Mach number
R	=	radial coordinate
St	=	Strouhal number (fD_j/U_j)
U_j	=	fully expanded jet velocity
u	=	streamwise velocity
v	=	vertical velocity
x	=	streamwise coordinate
y	=	vertical coordinate
a_∞	=	ambient sound velocity
p	=	pressure
ρ	=	density
p_∞	=	ambient pressure
ρ_∞	=	ambient density
p_{02}	=	total pressure behind a local normal shock
ω	=	vorticity

Presented as Paper 0500 at the 47th AIAA Aerospace Sciences Meeting, Orlando, FL, 5–8 January 2009; received 16 January 2009; revision received 10 April 2009; accepted for publication 15 April 2009.

*Mechanical Engineer; JhLiu@lcp.nrl.navy.mil. Member AIAA.
†Head, Center for Reactive Flow and Dynamical Systems; kailas@lcp.nrl.navy.mil. Fellow AIAA.
‡Aerospace Engineer; ravi@lcp.nrl.navy.mil. Associate Fellow AIAA.
§Graduate Student; David.munday@uc.edu. Member AIAA.
¶Distinguished Professor; Ephraim.Gutmark@uc.edu. Fellow AIAA.
**Professor; rlohner@gmu.edu. Associate Fellow AIAA.

I. Introduction

THERE is growing need to significantly reduce the noise generated by high-performance supersonic military aircraft. The noise generated during takeoff and landing on aircraft carriers has direct impact on shipboard health and safety issues. Noise complaints are increasing as communities move closer to military bases or when there are changes due to base closures and realignment. Furthermore, U.S. and international noise regulations and policies will have an impact on operations and training unless effective steps are taken to reduce the noise.

There is a significant amount of literature dealing with noise reduction in civilian subsonic aircraft. Some of the techniques found effective for subsonic jets could possibly be applied for noise reduction in supersonic jets. Many of these techniques use flow modifiers such as mechanical chevrons to enhance the mixing of the exhaust jet with the surroundings and reduce the jet noise. A distinct difference between current civilian aircraft engines and military aircraft engines is that military engines have low bypass ratios and high velocities and their noise is dominated by jet noise, especially shock-associated noise. This is because during flight near the ground or near an aircraft carrier, such as during takeoff or landing, the exhaust from the engines tends to be imperfectly (under/over) expanded. There is a need to focus on noise reduction under these operating conditions.

Although there are still fundamental questions about the source and mechanisms of noise generation in supersonic jets, significant progress has been made over the past few decades [1–8]. From the previous studies, it is known that the noise generated by an imperfectly expanded supersonic jet flow consists of discrete and high-amplitude screech tones, broadband shock-associated components, and mixing noise. The first two types of noise are related to the shock waves that are present in the high-speed jet flow. Although the mixing noise dominates in the downstream direction, the shock-associated noise elevates the overall noise level in the upstream direction. The screech tones are thought to arise due to a feedback loop involving the large-scale flow structures, their interactions with the shock-cell structure, and flow disturbances at or near the nozzle lip. Therefore, for the problem at hand, the simulations will need to

accurately capture shock waves, unsteady large-scale flow structures, and their interactions.

In spite of advances in computers and computing, direct numerical simulations of supersonic flows from realistic nozzles over the length and time scales of interest are not practical. On the other hand, large-eddy simulations (LES), which resolve the large scales and model the effect of small scales, have the potential to be a useful tool to investigate the flowfield and noise generation from supersonic jets. Substantial effort in advancing LES of jet flows has been made in the past decades [9–23]. Many of the pioneering studies (for example, [9–13]) have focused on simple subsonic round jets for the purposes of method and code development and to gain physical insight. Details of the nozzle geometries are not included, and inflow boundary conditions that specify mean velocity profiles and unsteady perturbations are used to provide conditions at the nozzle exit. A priori knowledge of nozzle exit conditions, however, is difficult to obtain in many practical applications, and the investigation of new noise reduction techniques requires the capability of accounting for the subtle effects of geometry variations on noise generation. Therefore, tools that can explicitly implement nozzle geometries have to be developed. Some examples of such endeavors can be found in [14–20]. Either structured or unstructured meshes with algorithms of finite difference or finite volume are used in these studies.

Papers on the applications of fully three-dimensional (3-D) LES to imperfectly expanded supersonic jet flows are very few. One challenge in addition to those seen in subsonic jets is the stability problem associated with the simulation of shock cells. Bodony et al. [21] and Lo et al. [22] have extended their methodologies used for subsonic jets [9,12] to the investigation of both perfectly and imperfectly expanded jets. Bodony et al. [21] consider only moderate pressure mismatches because no shock-capturing schemes were employed in their simulations. Lo et al. [22], on the other hand, apply a filtering process to keep the scheme stable. Some spurious numerical oscillations, however, are observed in their fully expanded jet simulations. Imamoglu et al. [23] use a high-order weighted essentially nonoscillatory scheme to simulate several imperfectly expanded jets. Screech modes are studied, and the computed shock-cell structure is in agreement with experiments and other published computations. Berland et al. [24] have used a low-dispersion and low-dissipation scheme with an explicit selective filtering to study the screech generation in a planar underexpanded jet. The flow development and the shock-cell structure are in agreement with experiments in the literature. The screech tones of fundamental and harmonic modes are observed and studied. The screech sound sources are also investigated. The preceding studies are rather academic in the sense that high-order schemes are used, simple grids are used, and real nozzle geometries are not included. Loh and Hultgren [16] have taken a different approach by using a space–time conservation-element and solution-element method using an unstructured hexahedral grid to study the screech noise in a circular underexpanded jet. The unstructured grid allows them to include the nozzle geometry, and the predicted shock-cell structure agrees well with the experiment results. However, the sound pressure levels are lower than the measurements. Shur et al. [19] and Viswanathan et al. [20] have taken a systematic approach and simulated a wide range of jet conditions, including several imperfectly expanded jets, with both round and beveled nozzles. They use multiblock structured grids to implement nozzle geometries and use upwind-biased high-order Roe schemes for the nonlinear terms in the Navier–Stokes equations. Their predictions of the noise levels are comparable with experimental results. No explicit modeling of subgrid scales is used in [16,19,20], in which flux limiters are employed to stabilize schemes.

The study reported in this paper is the numerical component of a joint research effort on supersonic jet noise with experiments being conducted at the University of Cincinnati and numerical simulations at the Naval Research Laboratory. Our technical approach is to design and fabricate representative nozzles, conduct experiments and acquire data, compare this information to validate the numerical simulations, and then use both experiments and simulations to understand sources of jet noise before investigating methods to reduce the noise. Thus, we focus on the predictions of the near-field flow and acoustic properties, especially the shock-associated noise properties. The nozzle geometries used in this research are representative of practical military engine nozzles. Such nozzles do not have smoothly varying contours designed by the method of characteristics to produce shock-free jet flows at the design condition. Instead, they typically have a conical converging section, a sharp throat, and a conical diverging section, which allows the area ratio to be changed in flight to adapt to local conditions and thrust requirements.

Because complicated nozzle geometries are involved, we use a finite-element-based flow solver to simulate the near field of supersonic jet flows. No explicit subgrid-scale model is used and the embedded flux limiter implicitly provides the modeling of subgrid scales. The present simulations are in the framework of monotonically integrated large-eddy simulations [25]. Because the nozzle boundary layer is very thin for supersonic flows with high Reynolds numbers, it takes a large amount of computational resource to resolve it directly and correctly. For the simulations reported in this paper, to simplify the problem, we have not included the boundary-layer development inside the nozzle. In addition, to avoid the introduction of arbitrary parameters and the possible parasitic noise created by artificial forcing [19], a steady inlet boundary condition is used. The nozzle lip rather than the nozzle boundary layer will be the major source to create disturbances to the shear layers in these jet simulations. Furthermore, considering that the viscous effects are not a key factor in noise generation in jet flows with high Reynolds numbers [13], viscous effects are not included. One of the goals of the current work is to assess the impact of ignoring the nozzle boundary layer and the viscous effects by directly comparing the results of the inviscid large-eddy simulations with experimental data.

II. Numerical Method

The unsteady, three-dimensional, inviscid, compressible flow equations are solved with a finite element flow code FEFLO using unstructured tetrahedral grids. The unstructured grids can accurately represent complicated geometries, such as the nozzle geometries used in this work. This capability is important when the geometry effect may have a large role on noise generation. The finite element version of a flux-corrected transport (FCT) algorithm (FEM-FCT) is used for the spatial discretization and a fourth-order Taylor–Galerkin scheme is used for the time integration [26]. FCT is ideal for simulating flows with embedded shocks, because it is conservative, monotone, and positivity-preserving [27]. This method has previously been used to simulate supersonic jet noise [28]. In addition, FCT is also a good option for linear wave propagation problems, for which the leading-order truncation error and the phase and amplitude errors are all fourth-order [29,30]. On the other hand, the leading-order truncation error for nonlinear problems is second-order in both limiting and nonlimiting (smooth) regions, and the error magnitude in smooth regions is much smaller [30]. The current methodology is very robust and does not require tuning of parameters.

A. Nozzle Geometry and Computational Domain

The nozzle geometry used in the simulations is shown in Fig. 1. The darker area is the nozzle flow path, and the lighter gray area is the nozzle wall. The details of the nozzle throat area are shown on the right-hand side of this figure. This nozzle is of the convergent–divergent type with a sharp throat and a conical diverging section. The diameters at the nozzle inflow, nozzle throat, and nozzle exit are 5.798, 2.640, and 2.868 in., respectively. The nozzle lip has a thickness of 0.02 in. The design Mach number for this nozzle is 1.5.

The computational domain is outlined in Fig. 2. Fine-grid cells are clustered around the nozzle exit and the jet plume. The area of fine mesh is divided into two major regions. The inner region, referred to as fine region I, is the most refined area, covering the jet plume to capture the energy-containing turbulence scales. This region includes the area near the nozzle exit and extends to $24D$ downstream. The radius of this region is $1.4D$ near the nozzle exit and

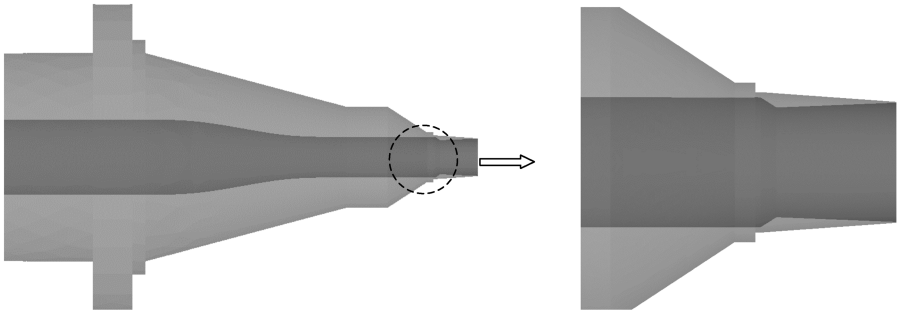

Fig. 1 Nozzle geometry. The figure on the right is an enlarged version of the area near the nozzle throat and the exit.

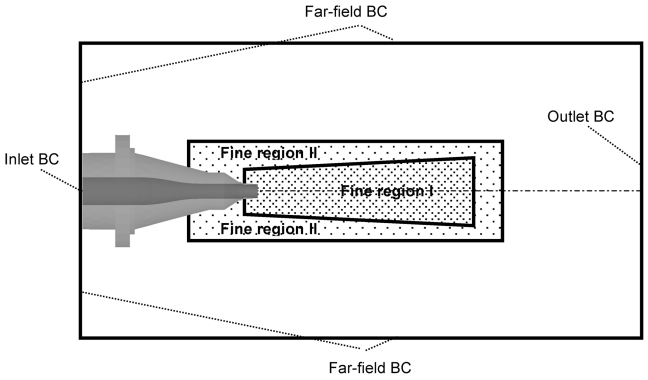

Fig. 2 Computational domain with descriptions of fine-grid regions and boundary conditions (BC).

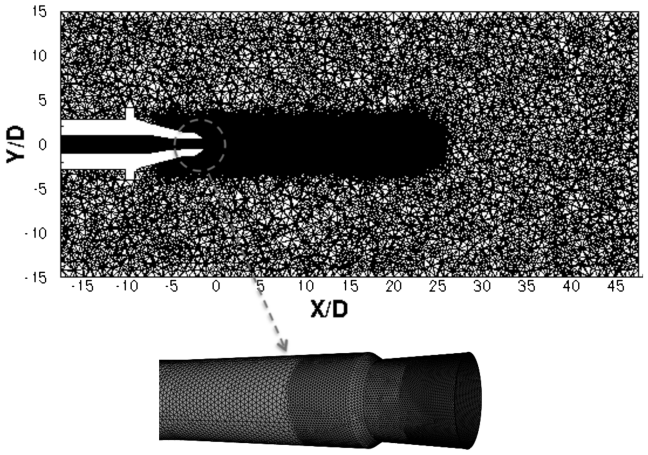

Fig. 3 Mesh distributions in the *x–y* plane and over the nozzle surface. Top: mesh in the *x–y* plane. Bottom: mesh of the nozzle inner surface near the nozzle exit.

1.9*D* at the end of this region. The cell size of 0.0345*D* is applied to the area further downstream without grid stretching. Near the nozzle exit, however, because the nozzle lip is very thin, the cell size is reduced gradually, as shown in the bottom figure of Fig. 3, to accommodate the lip thickness. But only one element is used around the lip to avoid a time-step size that is too small. The cell size inside the nozzle geometry increases as it approaches the inflow boundary. Because the propagation of sound waves in the frequency range of interest allows a little coarser cell size, the cell size in the outer region (fine region II in Fig. 2) increases to 0.065*D*. This region extends to 5*D* in the upstream area of the nozzle exit and to 24*D* in the downstream area with a radius of 3*D* in the radial direction. The top figure of Fig. 3 shows the mesh distribution in the *x–y* plane, in which the dark region is fine region II with fine region I buried within. Very coarse cell sizes are used in the far field and outflow boundaries to avoid wave reflections from these boundaries. The overall domain size is 15*D* in the radial direction, 17*D* in the upstream direction of the nozzle exit, and 47*D* downstream. This mesh, storing data at grid points, has roughly 11 million grid points and 65 million tetrahedral elements.

Characteristic boundary conditions are applied to both the far field and outflow boundaries, and the slip boundary condition is used for all solid surfaces. The total pressure is kept constant at the inlet of the nozzle.

B. Numerical Probes

Once a mature (i.e., quasi-steady) flowfield is established, the time-step size is kept constant and data are collected at small time intervals. Because the number of grid points is large, it is not realistic to save data at all points with a small time interval. Instead, the data at points on a Cartesian mesh, as shown in Fig. 4, are saved at regular time intervals (here, every 20 time steps). These points essentially serve as nonintrusive numerical probes in the flowfield. The distances between the neighboring probes are 0.2*D* in both the axial and radial directions for all cases except for NPR = 4.0, where the resolution is 0.1*D*. NPR stands for the nozzle pressure ratio between the nozzle total pressure and the ambient pressure. The Courant–Friedrichs–Lewy number is roughly 0.4 for all simulations.

C. Grid Resolution Study

Three grid resolutions are used in fine region I to evaluate the dependence of the key features of the flow on the grid. In addition to the grid resolution of 0.0345*D*, two coarser meshes that have cell sizes of 0.044*D* (25% coarser) and 0.061*D* (75% coarser) are also tested. Near the nozzle exit, however, cell sizes of all the three meshes are reduced gradually to have one element around the nozzle

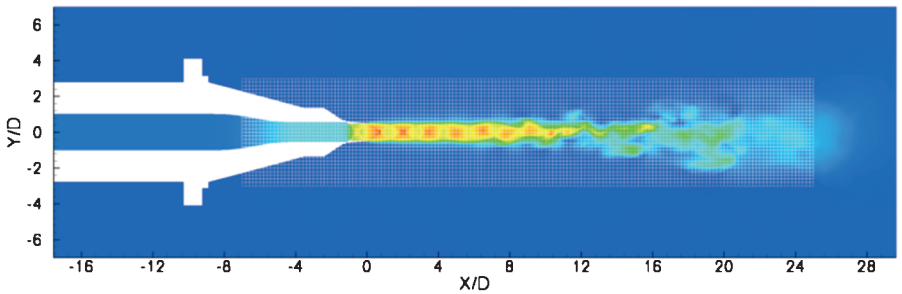

Fig. 4 Mesh of the numerical probes (in white), overlaid with an instantaneous Mach number distribution.

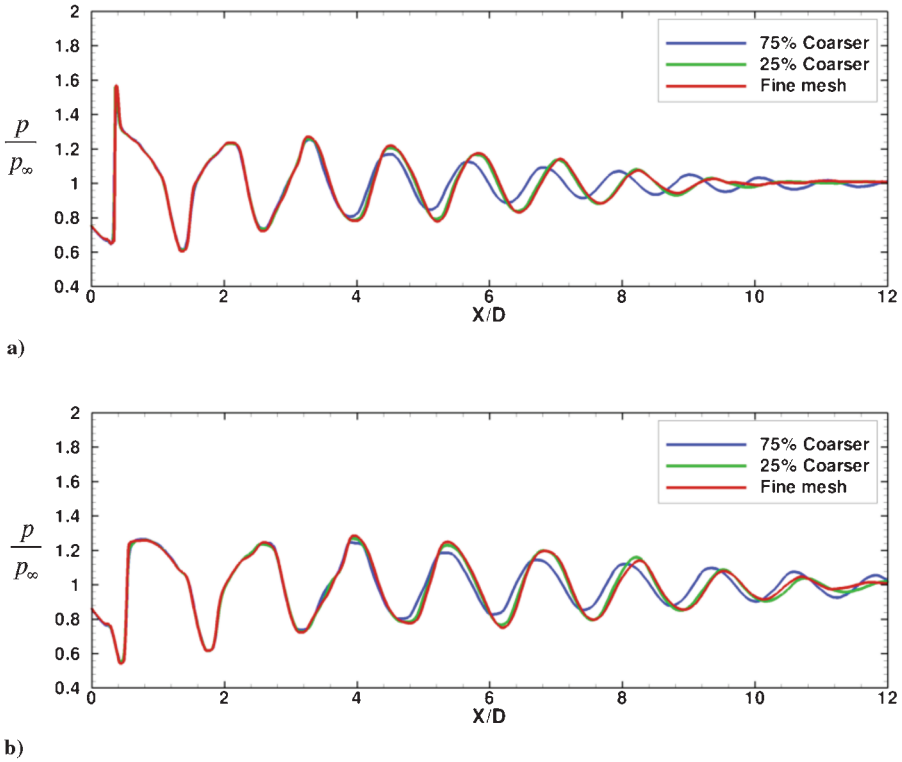

Fig. 5 Distributions of centerline static pressure predicted by three grid resolutions: a) NPR = 3.5 and b) NPR = 4.0.

lip. Thus, the grid resolution is similar for these three meshes within the range of 1.8D downstream of the nozzle exit, and the current grid resolution study only focuses on the region away from the nozzle exit. Figure 5 shows distributions of the centerline static pressure using the three meshes for one overexpanded case (NPR = 3.5) and one underexpanded case (NPR = 4.0). The agreement over the first two shock cells is very good for all meshes. This similar grid resolution near the nozzle exit should be responsible for the excellent

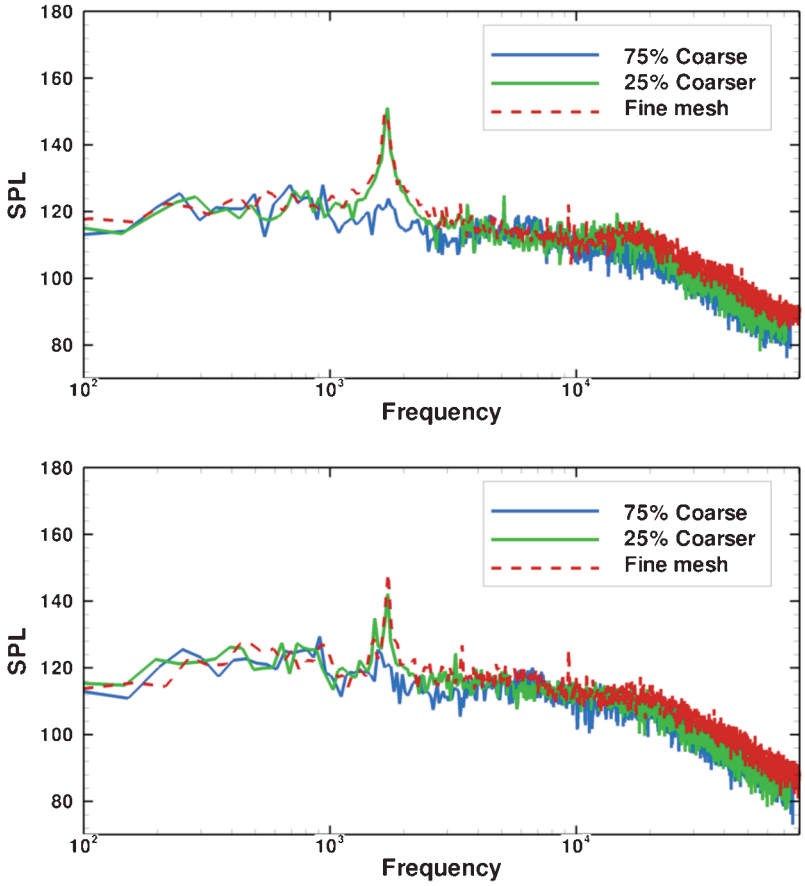

Fig. 6 Near-field SPL spectra at the location $x = 2.2D$ and $y = 1.0D$ by three grid resolutions: a) NPR = 3.5 and b) NPR = 4.0.

Table 1 Nozzle pressure ratios, jet Mach numbers, and jet velocities for all cases

	Case						
	1	2	3	4	5	6	7
NPR	2.5	3.0	3.5	3.7	4.0	4.5	5.0
M_j	1.22	1.36	1.47	1.51	1.56	1.64	1.71
U_j, m/s	373	403	426	434	444	459	471

agreement observed near the nozzle. However, roughly from the location of 4 jet diameters ($4D$), the results from the 75% coarser mesh start to deviate from the predictions of the two finer meshes. On the other hand, the difference between these two finer meshes is small. Figure 6 shows the noise spectra predicted by the three grid resolutions at the location of $2.2D$ downstream of the nozzle exit and $1D$ above the jet centerline. It can be seen that the two finer meshes predict a distribution of a similar shape and magnitude, and the finest mesh, as one would expect, predicts a slightly larger magnitude in the high-frequency range. However, the 75% coarser mesh predicts a much lower magnitude near the peak frequency. The comparison of the centerline results and the spectra data indicate that simulations using the two finer meshes have approximately achieved grid independence, at least at the level of mean flow quantities and acoustic spectra. To be on the conservative side and to capture more small-scale turbulence structures, the finest mesh of the three is used for all the results discussed subsequently.

III. Results and Discussion

From the one-dimensional isentropic flow analysis, the NPR at the design condition is roughly 3.7 for the nozzle geometry discussed in this paper. We have simulated jet conditions with NPRs ranging from 2.5 to 5.0 with an increment of 0.5 and also the design condition.

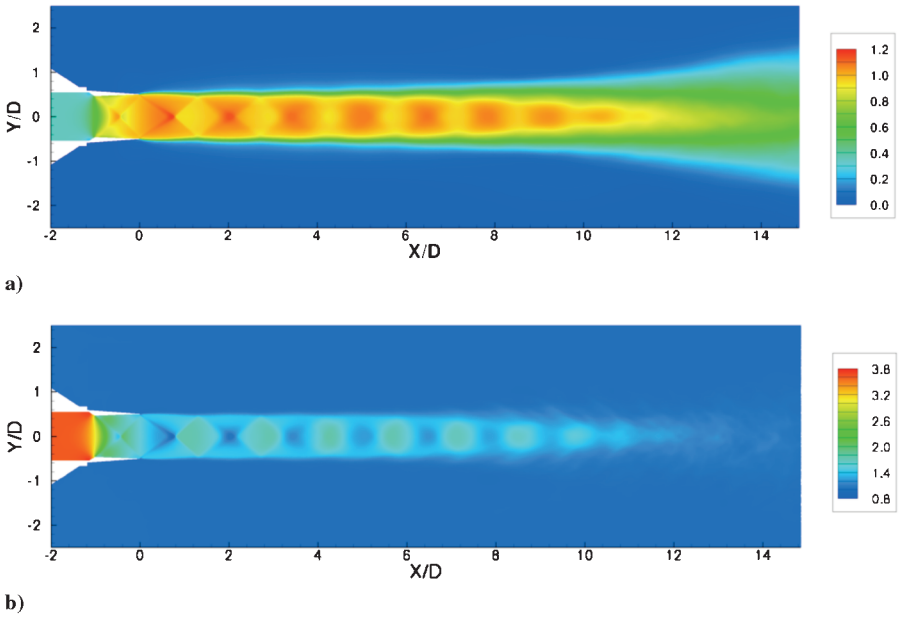

Fig. 7 Time-averaged distributions from the underexpanded jet simulation with NPR = 4.0: a) Streamwise velocity u/U_j and b) density ρ/ρ_∞.

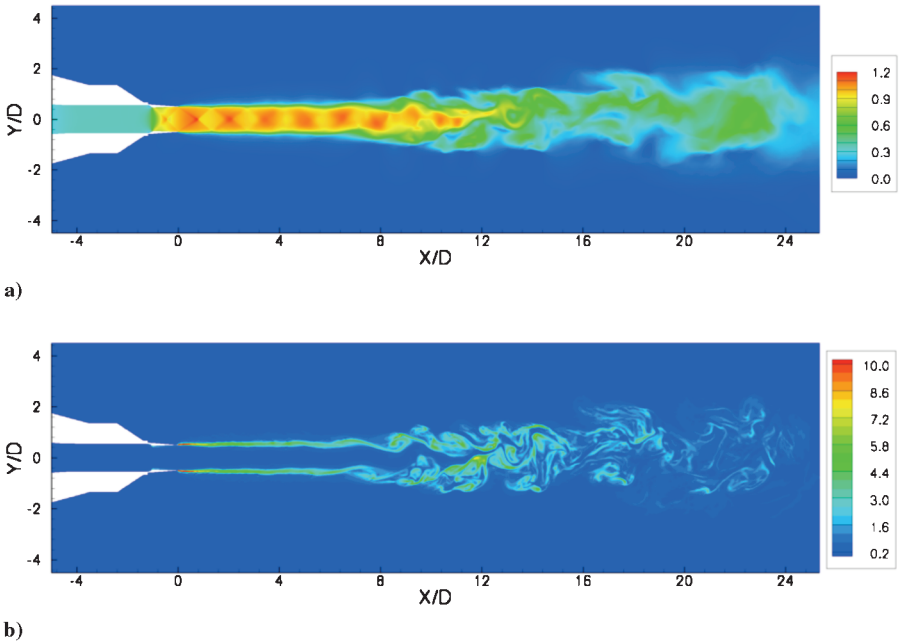

Fig. 8 Instantaneous velocity and vorticity distributions for the case with NPR = 4.0: a) Streamwise velocity u/U_j and b) vorticity magnitude $|\omega| \cdot (D/U_j)$.

NPR = 2.5, 3.0, and 3.5 are overexpanded cases and 4.0, 4.5, and 5.0 are underexpanded cases. The important parameters for these cases are given in Table 1. Because experimental data for this nozzle [31] are available for NPR = 3.5 and 4.0, the comparison between simulations and measurements will be made for these two conditions.

A. Results of the Flowfield

Figure 7 presents time-averaged velocity and density for the underexpanded case of NPR = 4.0. A train of shock cells is observed downstream of the nozzle exit, and the potential core ends near 12D for this pressure ratio. In addition, it can be seen that the expansion and compression waves start from inside the nozzle, slightly downstream of the throat. Figure 8 presents instantaneous streamwise velocity and the total vorticity magnitude. The shear layers of the jet start to roll up from about 7D, break down near 9D, and finally merge together around 12D, where the potential core ends.

The static pressure distributions near the nozzle exit are shown in Fig. 9 for all seven cases. It is clear that both the shock-cell size and spacing increase as the total pressure ratio increases. We have compared the shock-cell spacing with that given by Prandtl's vortex-sheet model [32] and from experimental measurements [31] in Fig. 10. The shock spacing given by the model [32] is in the form of

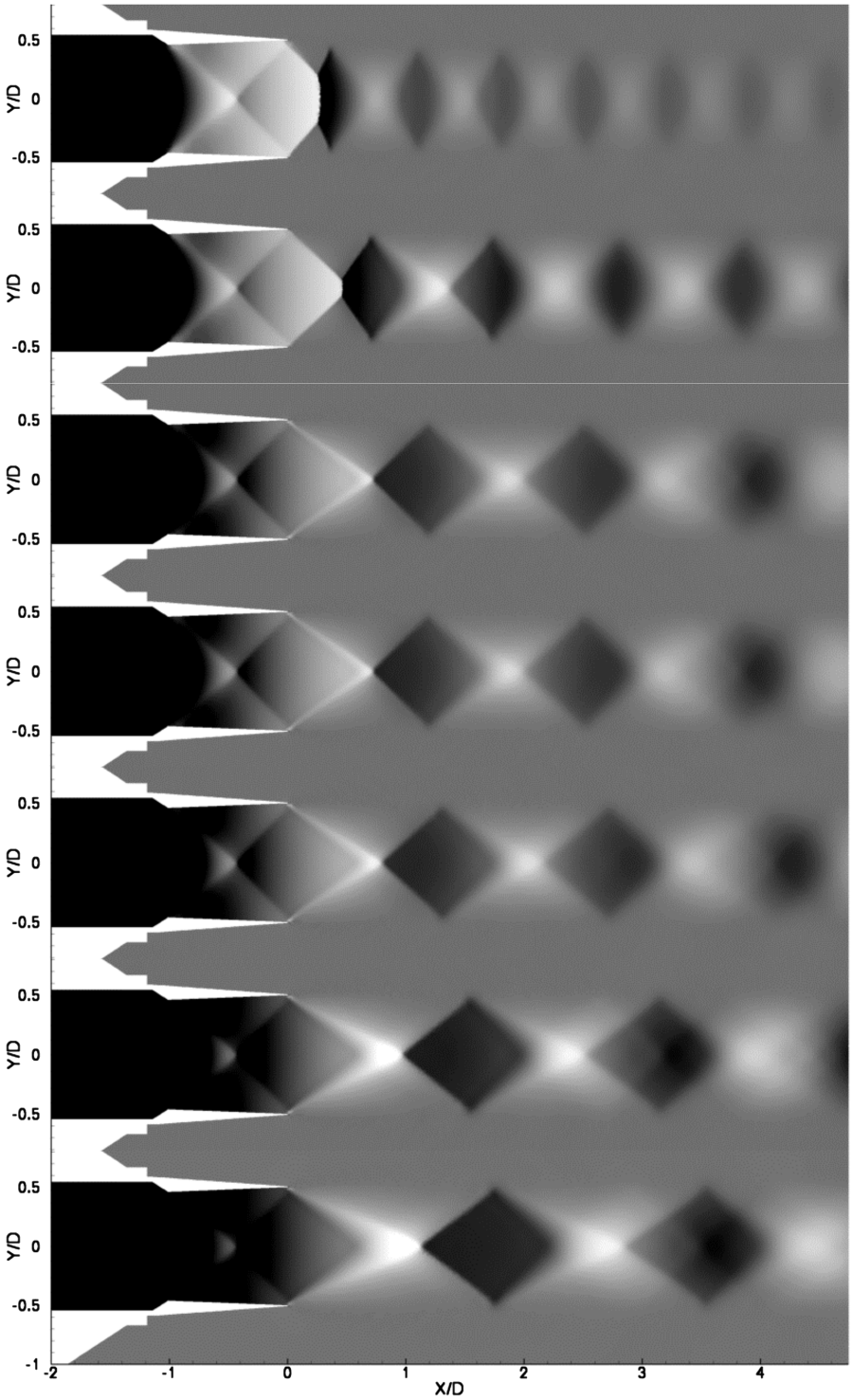

Fig. 9 Pressure distributions for the cases with NPR = 2.5, 3.0, 3.5, 3.7, 4.0, 4.5, and 5.0. The dark colors indicate high-pressure levels and white colors are low-pressure levels. The contour levels are in the range of [0.5P_∞, 1.4P_∞].

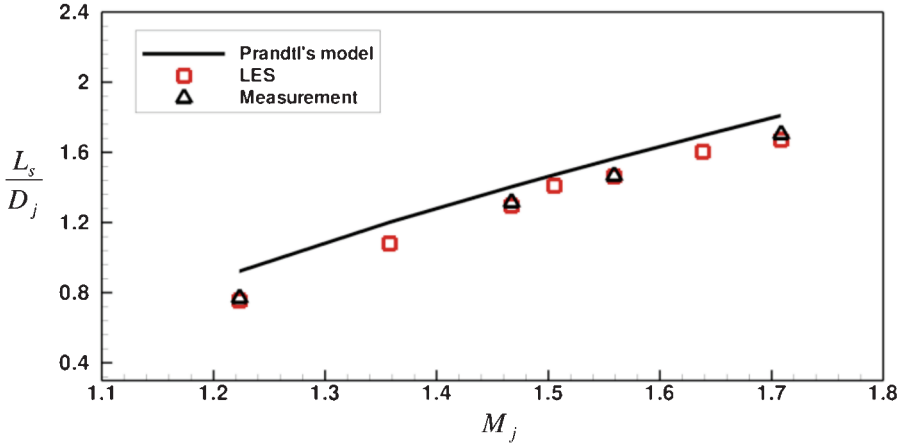

Fig. 10 Shock-cell spacing versus the jet Mach number. Line: Prandtl's vortex-sheet model [32]. Squares: LES. Triangles: Experimental measurements [31].

$$L_s = 0.4158\pi(M_j^2 - 1)^{1/2} D_j \tag{1}$$

Because the vortex-sheet model is valid only in the initial region immediately downstream of the nozzle in supersonic jets [2], only the first three cells are used to estimate the shock-cell spacing from the simulations and the experimental measurements. It can be seen that the comparison between LES and the experimental measurements is excellent, and the vortex-sheet model slightly overpredicts the shock-cell spacing. Figure 11 shows the centerline total pressure behind the local normal shock wave compared with that measured by a conical pitot pressure probe [31] for both the overexpanded case of NPR = 3.5 and the underexpanded case of NPR = 4.0. The reason we use the total pressure behind the local normal shock wave rather than the static pressure is because there are some ambiguities and difficulties in determining the axial location of the measured static pressure in supersonic flows using a conical pitot pressure probe. Though it is only a derived parameter of the flowfield, this total pressure provides information of the axial location, spacing, and strength of shock cells. We can see that these three quantities are all in good agreement between the computational and experimental results before the axial location of $7D$ for NPR = 3.5 and $8D$ for NPR = 4.0. Some differences, however, are seen after these axial locations, and the magnitudes predicted by numerical simulation are higher than

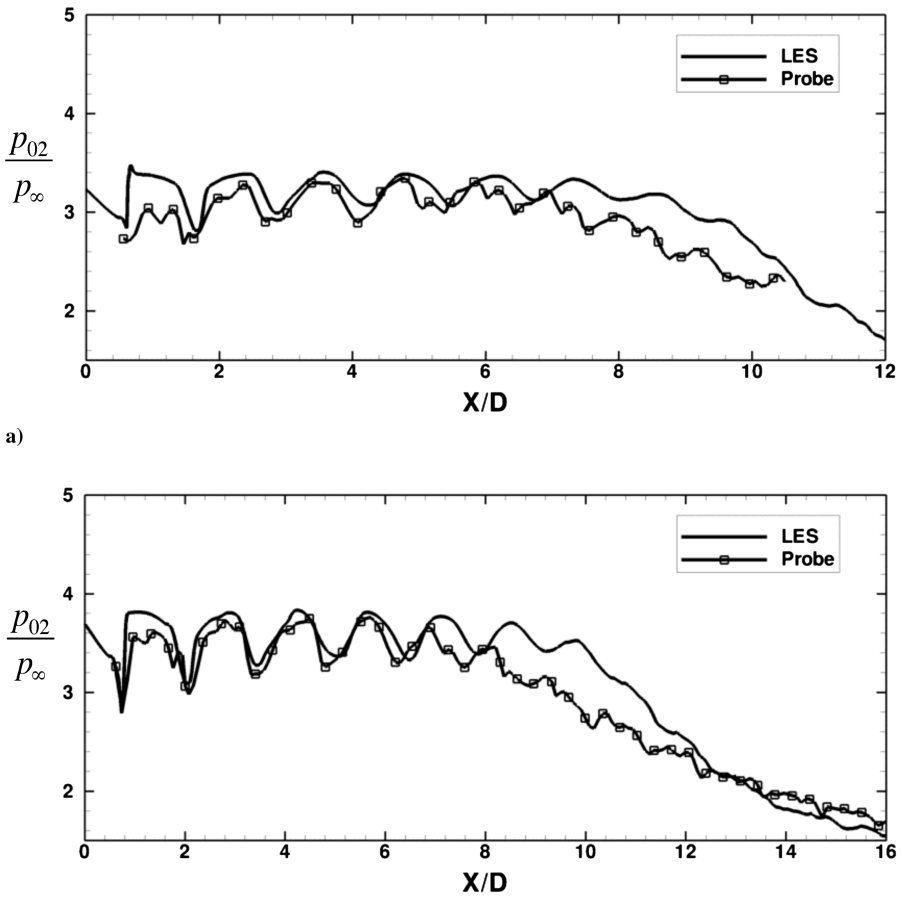

Fig. 11 Comparison of the centerline total pressure behind local normal shocks for a) the overexpanded jet with NPR = 3.5 and b) the underexpanded jet with NPR = 4.0.

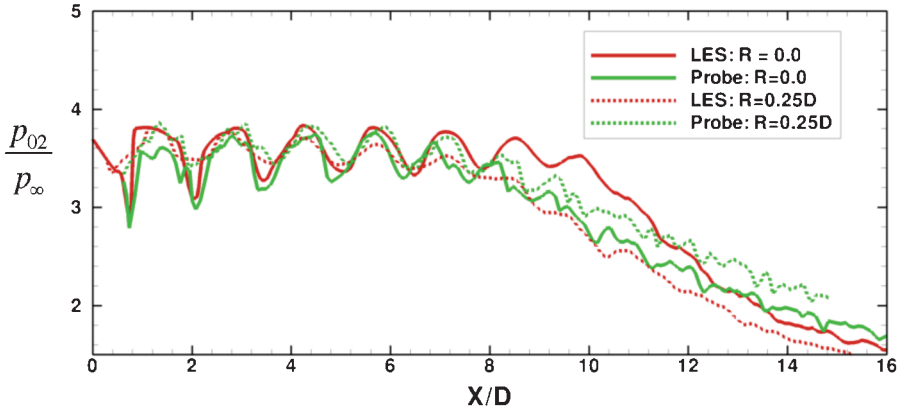

Fig. 12 Comparison of the centerline total pressure behind local normal shocks for NPR = 4.0 at two radial locations: centerline and 0.25*D* away from the centerline.

the experimental data before the end of the potential core, which is located roughly at 12*D*. Figure 12 shows results of both numerical simulation and measurement at two radial locations for NPR = 4.0. The numerical simulation predicts a total pressure at the centerline much higher than that at the radial location of 0.25*D* in the axial range of 8*D*–12*D*. In addition, as one would expect, the difference of the total pressure between the two radial locations decreases after the end of the potential core. However, the experimental data show a smaller difference of the total pressure between the two radial locations, and the two sets of data fall between LES predictions in the range of $x = 8D$–$12D$. Because the radial size of the potential core decreases quickly after $x = 8D$ for this underexpanded condition, small deviations from the centerline would produce larger differences. It appears that the probe may have deviated slightly from the centerline when it was used to measure the pressure there.

Although the pressure at the nozzle exit for the design condition (NPR = 3.7) is almost the same as the ambient pressure, a shock-cell pattern similar to that in the imperfectly expanded jets is still observed. On closer examination of the pressure distribution inside the nozzle shown in Fig. 9, we can see that the expansion and compression waves caused by the sharp contraction near the nozzle throat are responsible for the formation of the shock cells even at this design condition [31]. For these types of nozzle geometries, perfectly or ideally expanding the jets does not guarantee shock-free flows at the design condition, as one would normally expect. The centerline

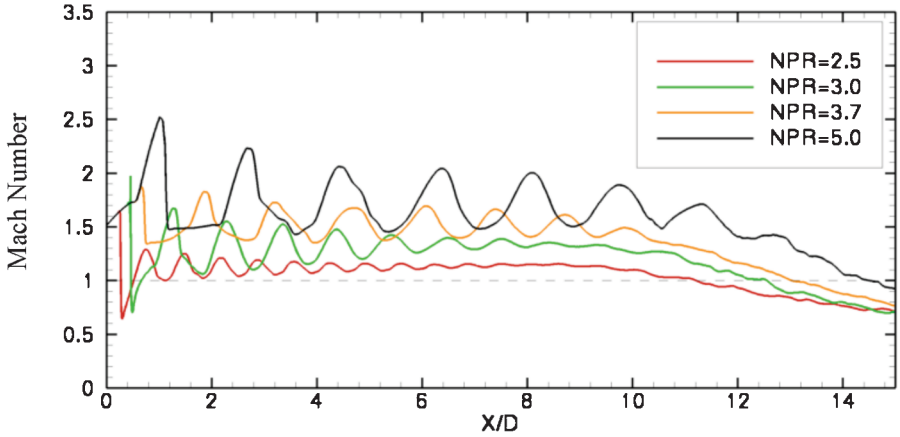

Fig. 13 Centerline Mach number distributions for several total pressure ratios.

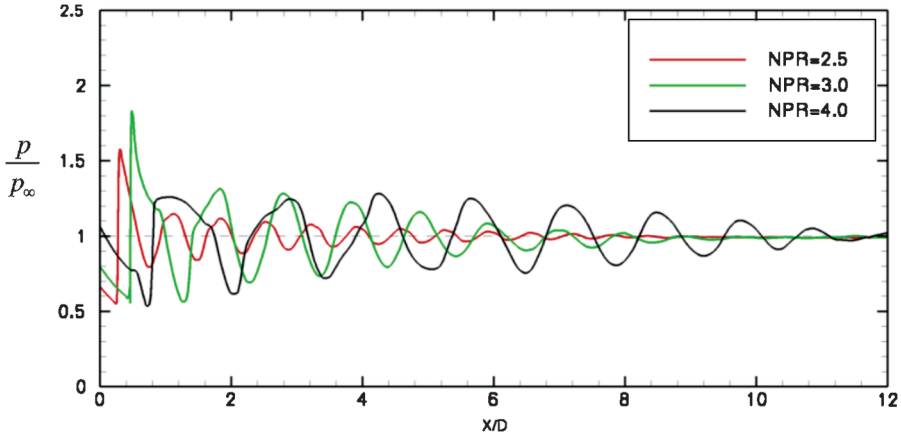

Fig. 14 Centerline pressure distributions for several total pressure ratios.

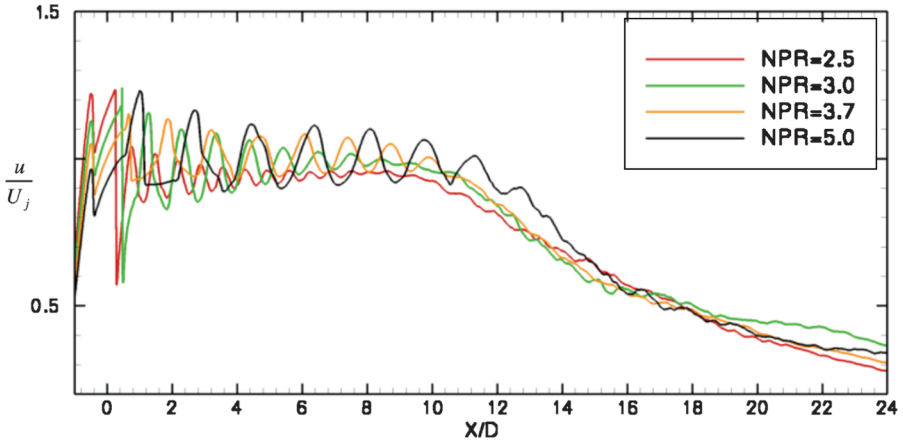

Fig. 15 Distribution of the centerline axial velocities scaled by U_j for several total pressure ratios.

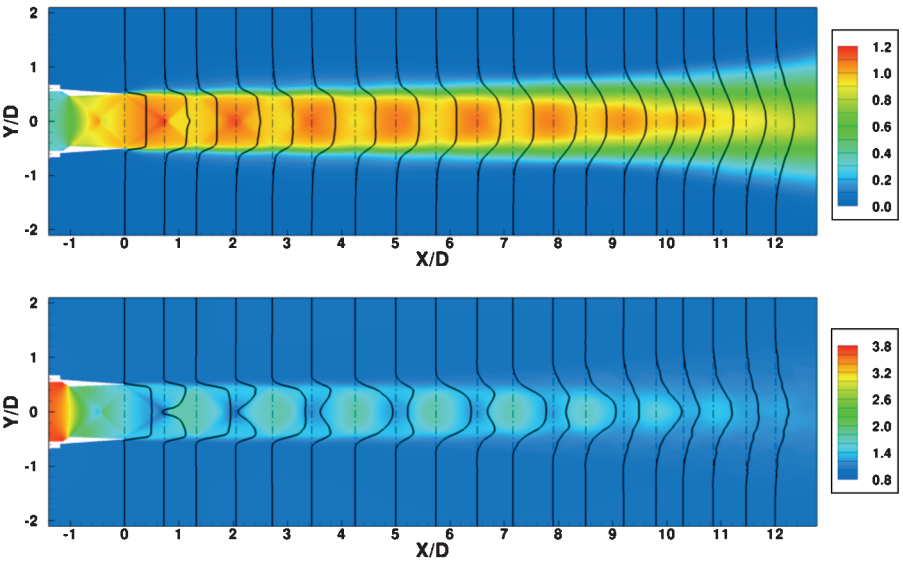

Fig. 16 Velocity and density profiles at centers of the high-pressure and low-pressure regions from the simulation with NPR = 4.0.

Mach number distributions for several total pressure ratios are shown in Fig. 13. There are areas in which the Mach number drops below 1.0 for overexpanded cases of NPR = 2.5 and 3.0. When we look into the pressure distributions for these two cases in Fig. 9, we can see that there is a Mach disk just behind the first expansion wave outside the nozzle exit. The radial width of the Mach disk increases as the total pressure ratio decreases.

Figure 14 shows the centerline static pressure distributions for these two overexpanded cases along with that of the case with NPR = 4.0. Large spikes of the static pressure are observed at the locations at which the Mach number is lower than 1.0. These types of large spikes were also observed in the overexpanded cases reported in Norum and Seiner's experimental study [33]. From the current simulations, it appears that Mach disks behind the first expansion wave cause these large spikes, and overexpanded cases are prone to having Mach disks if the total pressure ratio is much smaller than the nominally perfectly expanded condition.

Figure 15 is the centerline velocity distribution scaled by the fully expanded jet velocity U_j (the fully expanded value). It can be seen that the curves fluctuate around their jet velocity, except for the case of NPR = 2.5, in which case, the curve is somewhat lower than its fully expanded value. The energy loss over the strong Mach disk is probably responsible for this lower axial velocity. We can also see that the length of the potential core increases with the total pressure ratio, and the length of the shock train does not necessarily coincide with the length of the jet potential core. The shock cells weaken before the potential core breaks down when the

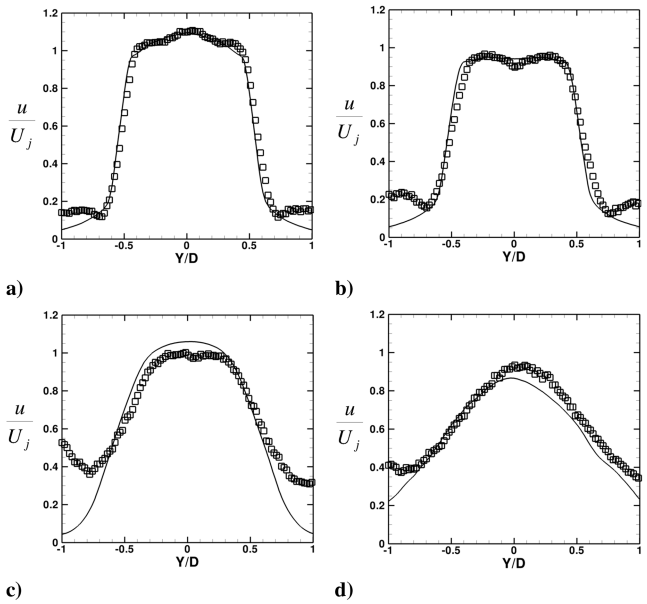

Fig. 17 Comparisons of streamwise velocity profiles at four axial locations for the case with NPR = 4.0. Lines: LES, symbols: measurement: a) $x = 2.15D$ (center of the second low-pressure region), b) $x = 2.8D$ (center of the second high-pressure region), c) $x = 7.7D$, and d) $x = 12D$.

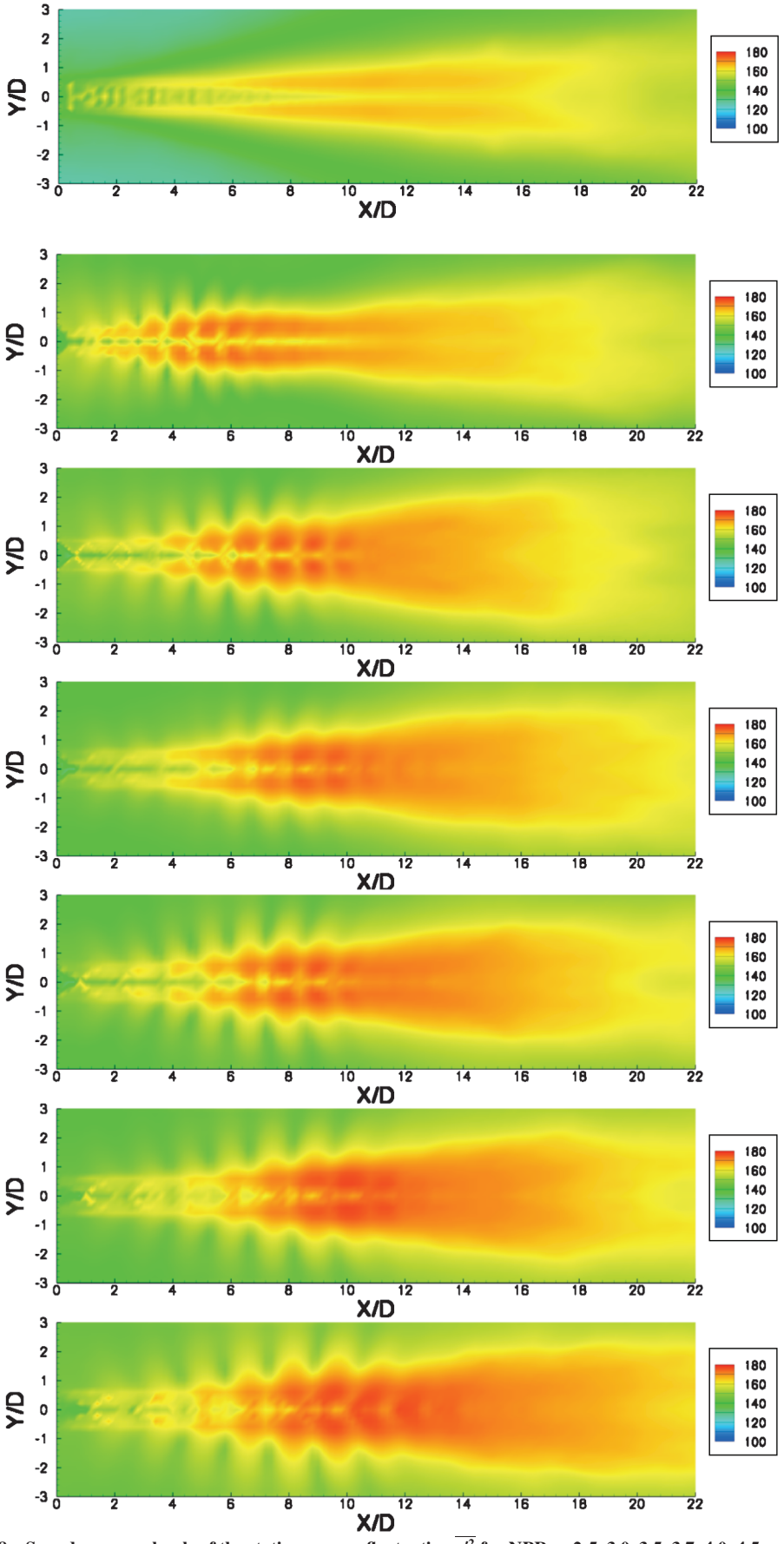

Fig. 18 Sound pressure levels of the static pressure fluctuation $\overline{p'^2}$ for NPR = 2.5, 3.0, 3.5, 3.7, 4.0, 4.5, and 5.0.

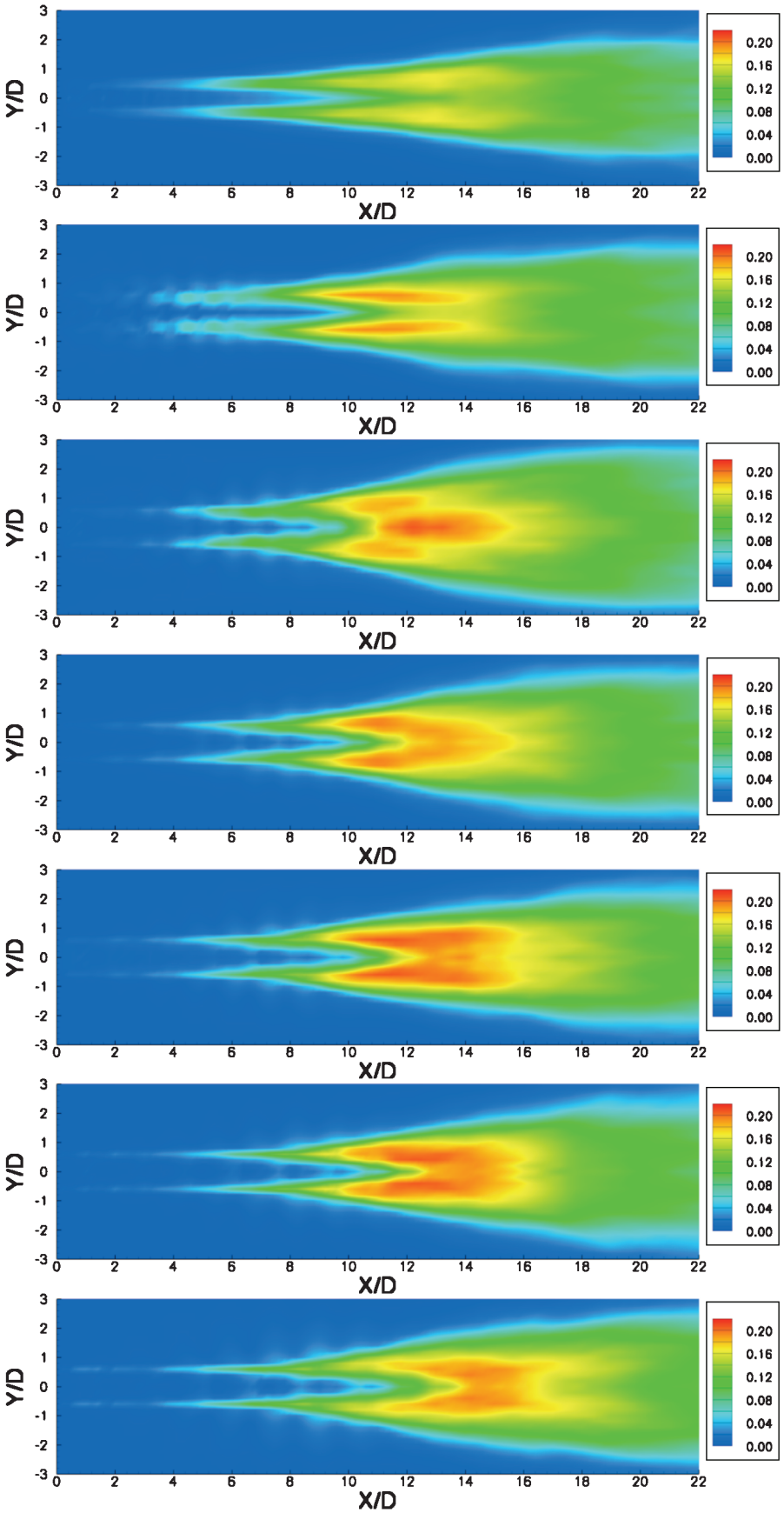

Fig. 19 Turbulence normal stress $(\overline{u'u'})^{1/2}/U_j$ for NPR = 2.5, 3.0, 3.5, 3.7, 4.0, 4.5, and 5.0.

total pressure ratio is low, such as those of NPR = 2.5 and 3.0. For high total pressure ratios, such as NPR = 5.0, shock cells remain much longer and are seen even after the potential core starts breaking down.

The radial profiles of the streamwise velocity and the density at the centers of both low-pressure regions and high-pressure regions are shown in Fig. 16 for several axial locations. The profiles at the centers of high-pressure regions are similar to those of subsonic jet flows, but

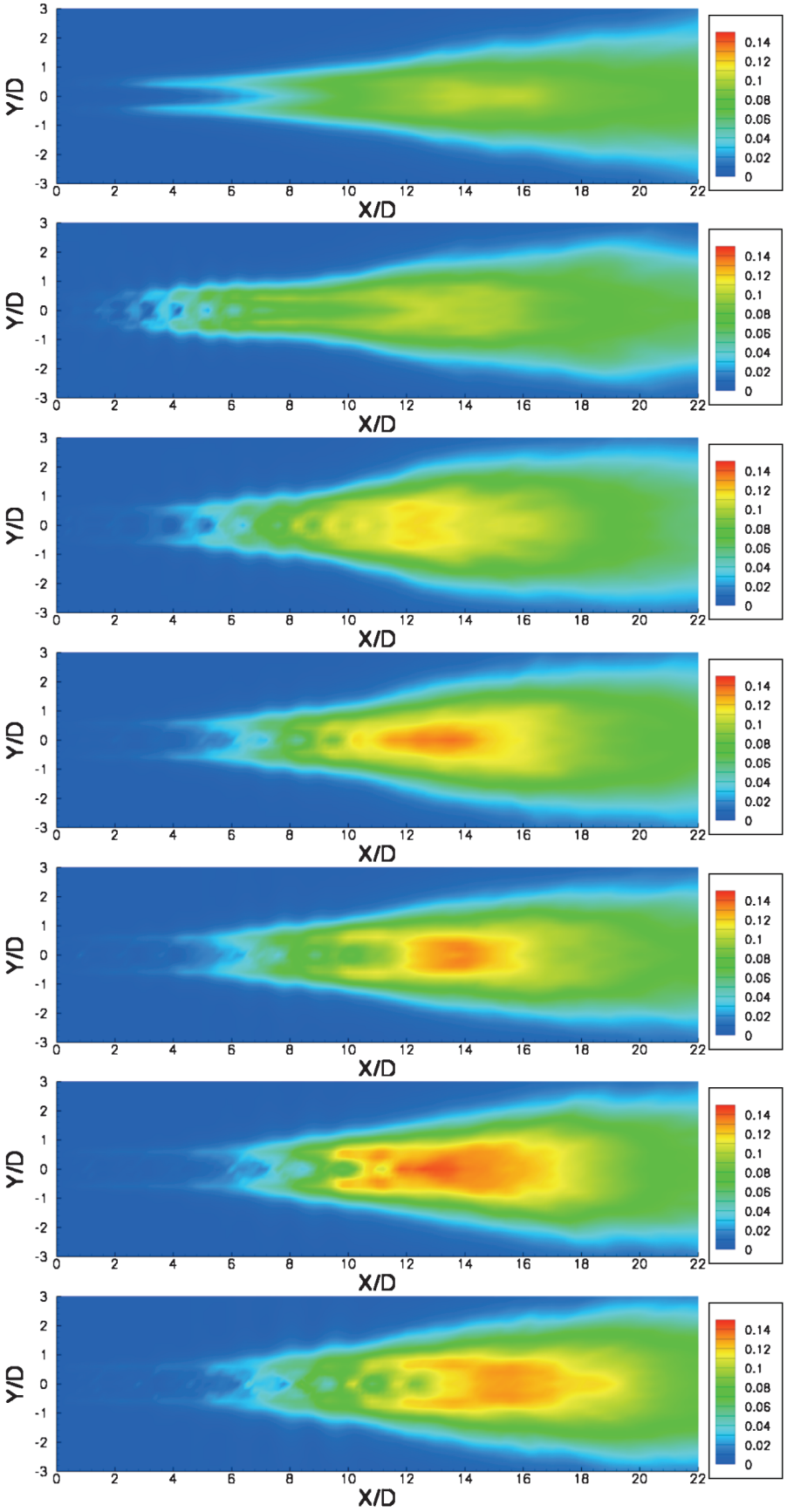

Fig. 20 Turbulence normal stress $(\overline{v'v'})^{1/2}/U_j$ for NPR = 2.5, 3.0, 3.5, 3.7, 4.0, 4.5, and 5.0.

the profiles at the centers of low-pressure regions have features that are quite different. A large dip of the density (pressure should be similar) is seen at the center, and a small peak is seen in the Mach number profiles. As the jet develops further downstream, the difference between these two types of profiles decreases and all of them evolve toward the fully developed profile. In addition, several radial profiles of the streamwise velocity are compared with data from particle image velocimetry measurements in Fig. 17. It can be

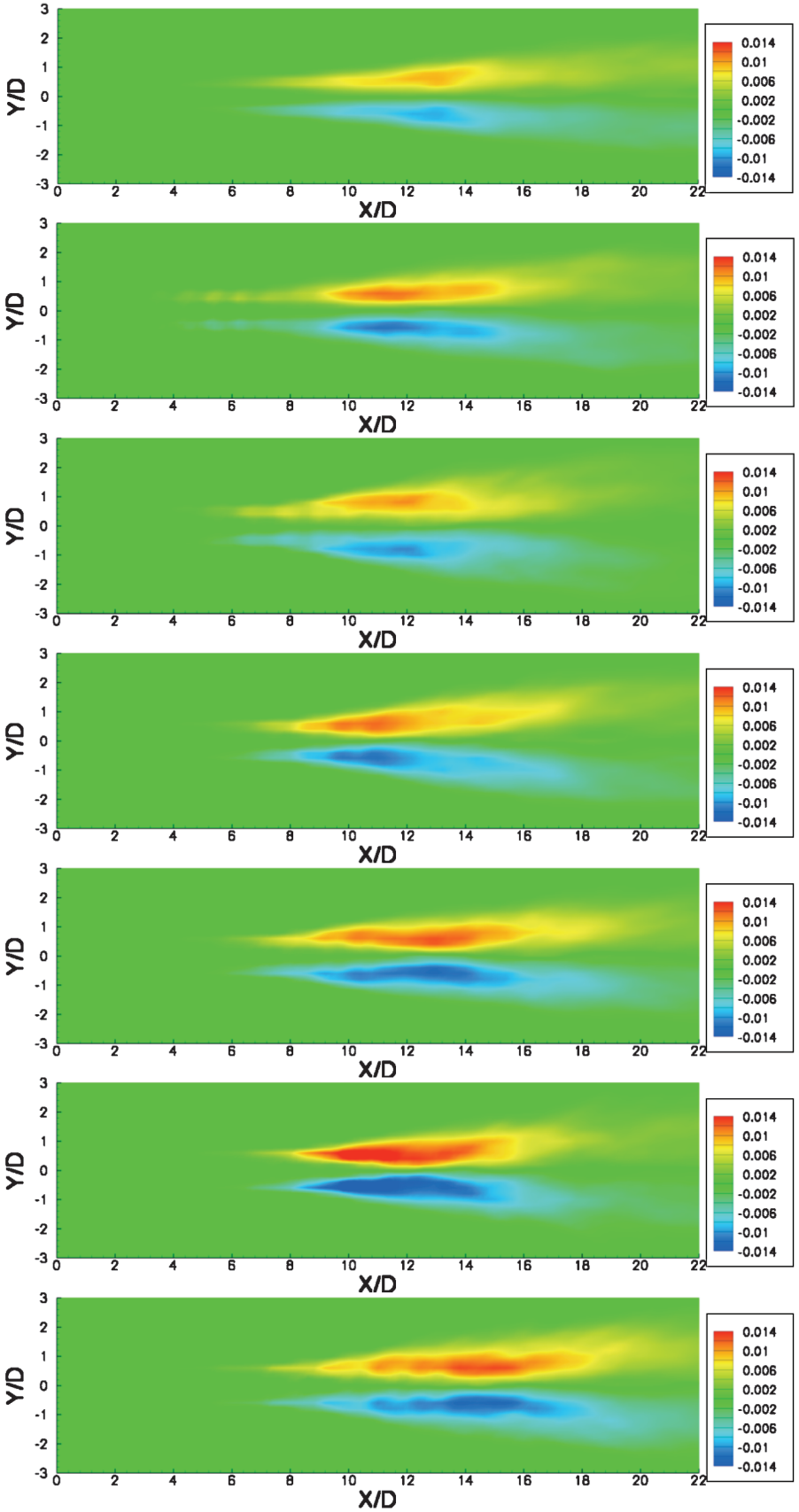

Fig. 21 Turbulence shear stress $\overline{u'v'}/U_j^2$ for NPR = 2.5, 3.0, 3.5, 3.7, 4.0, 4.5, and 5.0.

seen that the comparison inside the jet core is very good. Outside the jet core, however, there are some differences, but there are larger uncertainties in the measurements at these locations due to poor seed density outside the jet.

The intensities of the static pressure fluctuations are shown in Fig. 18. The results are averaged over a time interval of 200–300 convection time units (D/U_j). A phase average over the positive and negative y is also used, which produces symmetrical distributions in

the y direction. The sound pressure level of $\overline{p'^2}$ in decibels, rather than $\overline{p'^2}$ itself, is plotted in this figure to magnify the pressure fluctuations that are at the acoustic levels. It can be seen that large intensities of pressure fluctuations are seen in regions occupied by shock cells and also in the mixing region. The prominent features are the wavy structures in all cases except in the overexpanded case with NPR = 2.5, which is the only case in which a screech tone is not observed in the simulations. Thus, these wavy structures should be associated with either the generation or propagation of screech tones. The locations of wavy structures are closer to the nozzle exit in overexpanded cases, and the radial extent of these structures increase slightly as the total pressure ratio increases, except at the design condition, in which the strength is the weakest. In addition, the mixing region with large pressure fluctuations extends further downstream as the total pressure increases. Although the screech tone is not observed in the case of NPR = 2.5, the shock cells clearly contribute to pressure fluctuations in the jet core, even for this case.

The normalized turbulence normal stresses of the axial and radial components, $(\overline{u'u'})^{1/2}$ and $(\overline{v'v'})^{1/2}$, are shown in Figs. 19 and 20. As expected, the magnitude near the nozzle exit is small because both the inflow turbulence and nozzle boundary layers are not included. However, large magnitudes of these normal stresses are found near the potential cores to several diameters downstream. In our simulations, the turbulence is mainly introduced by disturbances from the nozzle lip and the instabilities propagating and growing inside the jet shear layers. Similar to that observed in a subsonic jet flow, the breakdown of the shear layers and the entailed mixing process are key contributors to the large magnitudes of turbulence fluctuations. The magnitude of the axial normal stress is found to be slightly more than 20% of the jet velocity and the magnitude of the radial component is around 15%. The peak values of the radial component are located near the jet axis, but those of the axial component, except for NPR = 3.5, are off the center. Overall, the magnitudes of turbulence fluctuations are lower in overexpanded cases than those in underexpanded cases. This trend is more apparent in the distributions of the radial component.

The shock cells and the screech tones have also contributed to the normal stresses, as indicated by the visible intensities in regions in which shock cells are present and also by the weak wavy structures. This shock-introduced contribution is more visible in the distributions of the radial component in overexpanded cases. On the other hand, shock cells have much less impact on the shear stress $\overline{u'v'}$, as shown in Fig. 21. This shear stress is mainly observed in the mixing region for all cases.

B. Results of the Near-Field Sound Pressure Level

The near-field sound pressure level (SPL) spectra at each numerical probe location is calculated and compared with results from the measurements. Figure 22 presents the near-field SPL spectra at the location of $x = 2.2D$ and $y = 1.0D$ for two jet conditions: NPR = 3.5 and 4.0. Similar to what we have observed previously, a screech tone is seen in both experiments and simulations. Both the intensity and frequency are in good agreement between the numerical predictions and the measurements. The screech frequency agrees very well with the experimental data for the overexpanded case, but for the underexpanded case it is slightly larger. If we examine the peak frequency closely, we would find that the experimental data show two peaks around the screech frequency for both overexpanded and underexpanded conditions, and the first peak has a dominant magnitude. The numerical simulation for the underexpanded condition also predicts two peaks with frequencies similar to those shown in experimental data, but the dominant magnitude is found at the second peak, rather than at the first one. We are not sure why the measurement and simulation show a different preference of the dominant peak frequency for the underexpanded condition. The overexpanded case, on the other hand, shows only one peak frequency, and this peak frequency coincides with the first peak shown in the experimental data. Similar trends are also observed for other overexpanded and underexpanded conditions. The design condition, however, shows two peaks with comparable

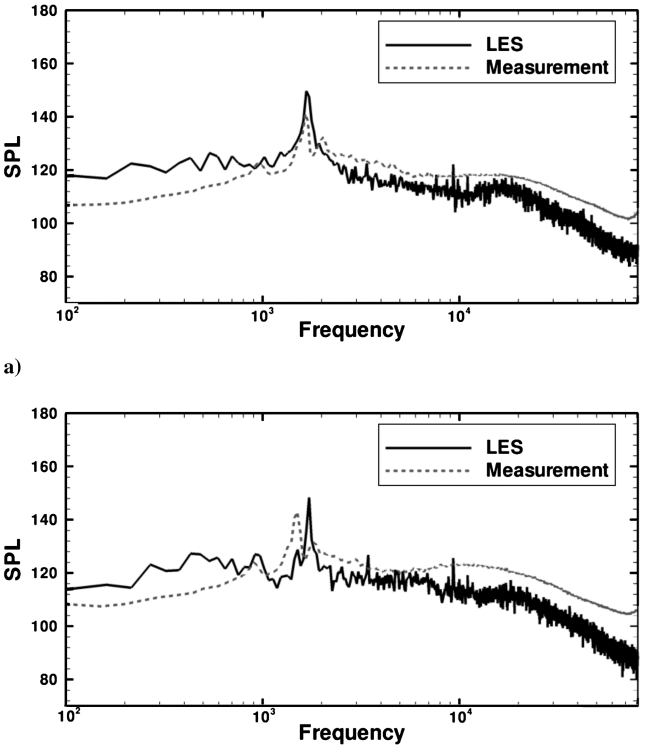

Fig. 22 Comparison of the near-field SPL spectra at the location $x = 2.2D$ and $y = 1.0D$ for a) the overexpanded jet case with NPR = 3.5 and b) the underexpanded jet case with NPR = 4.0.

magnitudes around the screech frequency. The wavelengths of the dominant screech tones are plotted in Fig. 23 along with the experimental data and the theoretical prediction of Tam et al. [34]. One exception is made for the design condition in which both peaks are plotted in this figure. The ambient sound speed is used as the wave propagation speed to compute the wavelength from the frequency. The results agree well among the three approaches. The simulation results jump slightly downward in the underexpanded region, in which a better agreement is seen between LES results and the theoretical prediction. The screech tones are found in helical modes, but it appears that the overexpanded and underexpanded cases are in two different helical modes, similar to what was found in [35] for an axisymmetric supersonic jet from a convergent–divergent nozzle.

The intensities predicted by numerical simulations in the low-frequency range are slightly higher than the experimental data, but they are slightly lower in the high-frequency range. From what was shown in the grid resolution study, we can expect that a finer grid resolution would reduce the difference in the high-frequency range. In addition, the intensities of screech tones are 4–7 dB higher than those of the experimental data. It is well known that predicting

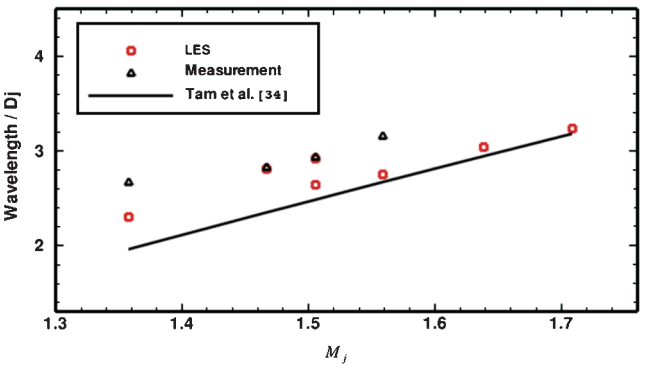

Fig. 23 Wavelengths of screech tones versus fully expanded jet Mach number.

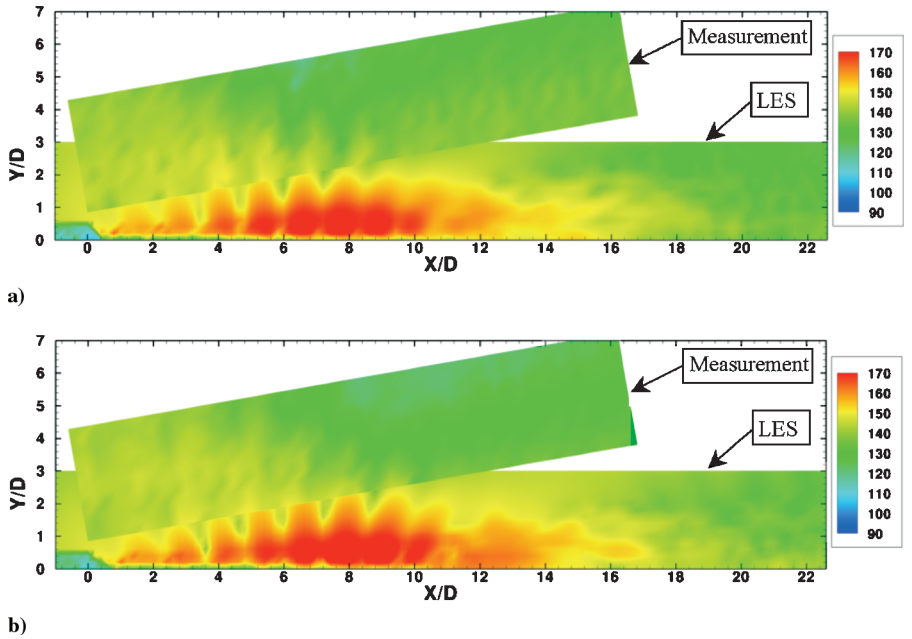

Fig. 24 Comparison of intensities of screech tones predicted by numerical simulations and measurements: a) the overexpanded case with NPR = 3.5 (peak frequency is 1666 Hz for LES and 1650 Hz for measurement) and b) the underexpanded case with NPR = 4.0 (peak frequency is 1720 Hz for LES and 1500 Hz for measurement).

screech intensities is difficult, because they are sensitive to minor differences of conditions, and we would expect that this sensitivity to be more pronounced in the near field than in the far field. There are quite a few differences between conditions used in numerical simulations and those in measurement: for example, the nozzle boundary layer, inlet turbulences, numerical truncation errors, nozzle lip resolution, and more. So far, we are not sure of the main factor responsible for the differences between LES and experimental data. But as a whole, the comparison between the LES predictions and experimental data is good.

The SPL distributions at the peak frequencies for NPR = 3.5 and 4.0 are shown in Fig. 24, along with the results of the measurements. Because it is difficult to measure sound pressure level near the jet axis experimentally, the data inside the potential core are not available from the measurements. On the other hand, because the fine grid is restricted to a region with a small radius due to finite computational resources, the overlap between the simulation and the measurements is small. However, because our target is to investigate the shock-associated noises, this small overlap region is sufficient for us to validate numerical simulations. Both LES and experimental data show banded structures at peak frequencies. The transition from the simulation to measurement is very smooth in the case of NPR = 3.5, in which both the magnitude and pattern are in good agreement. On the other hand, we would not expect the transition in the case of NPR = 4.0 to be as good as it is in NPR = 3.5, because the peak frequencies of these two approaches, as shown in earlier Fig. 22b, are roughly 200 Hz different. The magnitude is higher in the simulation, and the wavelength of the banded structure is smaller than that of the experimental data. As a whole, however, the overall agreement is still reasonable for this underexpanded condition.

IV. Conclusions

Large-eddy simulations of imperfectly expanded jet flows from a convergent–divergent nozzle with a design Mach number of 1.5 have been carried out. Jet conditions with various total pressure ratios from overexpanded to underexpanded cases have been investigated. Spacing of the shock cells and the length of the potential core increase as the total pressure ratio increases and are in good agreement with the experimental data and previous results from theoretical modeling. In addition, the streamwise velocity profiles also agree well with the experimental measurements.

A Mach disk is observed for overexpanded jet conditions when the total pressure ratios are relatively small. This Mach disk is responsible for the large pressure spike at the first shock cell. Unexpectedly, weak shock cells are also observed at the design condition. Results from the simulations have identified the cause for these waves to be the sharp contraction at the nozzle throat, which was used to make the nozzle representative of realistic military engine nozzles. Hence, these studies suggest that the flowfields from realistic engine nozzles are not likely to be shock-free under any operating condition. This lends further importance to the study of nonideally expanded jet flows. In addition, the intensities of the pressure fluctuations show wavy structures for nozzle pressures at which screech tones are observed. The turbulence intensities are lower in overexpanded cases than in underexpanded cases, but the contribution to normal stresses from shock-cell fluctuations and from screech tones are more visible in overexpanded cases. The shock cells have much less impact on the shear stress $\overline{u'v'}$.

Pressure distributions and near-field noise intensities obtained from the simulations show very good agreement with those obtained from the experimental measurements. This good agreement shows that LES and measurements can play complementary roles in the investigation of the noise generation from supersonic jet flows. In addition, such good agreement also indicates that the boundary layer at the nozzle exit and viscous effects, which are not included in the present simulations, may not be the most important factors in the noise generation of shock-containing jet flows with very high Reynolds numbers.

Acknowledgments

This work has been sponsored by the Strategic Environmental Research and Development Program (SERDP) and the NRL 6.1 Computational Physics Task Area. The authors also gratefully thank Steve Martens from GE Global Research for his guidance and advice in the design of realistic test cases and general insights into nozzle flow and acoustics.

References

[1] Tam, C. K. W., and Tanna, H. K., "Shock-Associated Noise of Supersonic Jets from Convergent-Divergent Nozzles," *Journal of Sound and Vibration*, Vol. 81, No. 3, 1982, pp. 337–358. doi:10.1016/0022-460X(82)90244-9

[2] Tam, C. K. W., "Jet Noise Generated by large Scale Coherent Motion, Aeroacoustics of Flight Vehicles: Theory and Practice," Vol. 1, edited by H. H. Hubbard, NASA RP-1258, 1991, pp. 311–390.
[3] Tam, C. K. W., "Supersonic Jet Noise," *Annual Review of Fluid Mechanics*, Vol. 27, 1995, pp. 17–43.
[4] Norum, T. D., and Seiner, J. M., "Broadband Shock Noise from Supersonic Jets," *AIAA Journal*, Vol. 20, No. 1, 1982, pp. 68–73. doi:10.2514/3.51048
[5] Seiner, J. M., "Advances in High Speed Jet Aeroacoustics," AIAA Paper 84-2275, 1984.
[6] Raman, G., "Advances in Understanding Supersonic Jet Screech: Review and Perspective," *Progress in Aerospace Sciences*, Vol. 34, Nos. 1–2, 1998, pp. 45–106. doi:10.1016/S0376-0421(98)00002-5
[7] Umeda, Y., and Ishii, R., "On the Sound Sources of Screech Tones Radiated from Choked Circular Jets," *Journal of the Acoustical Society of America*, Vol. 110, No. 4, 2001, pp. 1845–1858. doi:10.1121/1.1402620
[8] Panda, J., "Identification of Noise Sources in High Speed Jets via Correlation Measurements—A Review," AIAA Paper 2005-2844, 2005.
[9] Bodony, D. J., and Lele, S. K., "On Using Large-Eddy Simulation for the Prediction of Noise from Cold and Heated Turbulent Jets," *Physics of Fluids*, Vol. 17, 2005, Paper 085103. doi:10.1063/1.2001689
[10] Bogey, C., and Bailly, C., "Effects of Inflow Conditions and Forcing on Subsonic Jet Flows and Noise," *AIAA Journal*, Vol. 43, No. 5, 2005, pp. 1000–1007. doi:10.2514/1.7465
[11] Freund, J. B., "Noise Sources in a Low-Reynolds-Number Turbulent Jet at Mach 0.9," *Journal of Fluid Mechanics*, Vol. 438, 2001, pp. 277–305. doi:10.1017/S0022112001004414
[12] Uzun, A., Blaisdell, G. A., and Lyrintzis, A. S., "Coupling of Integral Acoustics Methods with LES for Jet Noise Prediction," *International Journal of Aeroacoustics*, Vol. 3, No. 4, Oct. 2004, pp. 297–346. doi:10.1260/1475472043499290
[13] Bodony, D. J., and Lele, S. K., "Current Status of Jet Noise Predictions Using Large-Eddy Simulation," *AIAA Journal*, Vol. 46, No. 2, Feb. 2008, pp. 364–380. doi:10.2514/1.24475
[14] DeBonis, J. R., and Scott, J. N., "A Large-Eddy Simulation of a Turbulent Compressible Round Jet," *AIAA Journal*, Vol. 40, No. 7, July 2002, pp. 1346–1354. doi:10.2514/2.1794
[15] Andersson, N., Eriksson, L., and Davidson, L., "Large-Eddy Simulation of Subsonic Turbulent Jets and Their Radiated Sound," *AIAA Journal*, Vol. 43, No. 9, 2005, pp. 1899–1912. doi:10.2514/1.13278
[16] Loh, C. Y., and Hultgren, L. S., "Near-Field Noise Computation for a Supersonic Circular Jet," AIAA Paper 2005-3042, 2005.
[17] Vuillot, F., Lupoglazoff, N., and Rahier, G., "Double-Stream Nozzles Flow and Noise Computations and Comparisons To Experiments," AIAA Paper 2008-9, 2008.
[18] Xia, H., Tucker, P. G., and Eastwood, S., "Towards Jet Flow LES of Conceptual Nozzles for Acoustic Predictions," AIAA Paper 2008-10, 2008.
[19] Shur, M. L., Spalart, P. R., Strelets, M. K., and Garbaruk, A. V., "Further Steps in LES-Based Noise Prediction for Complex Jets," 44th Aerospace Sciences Meeting and Exhibit, Reno, NV, AIAA Paper 2006-0485, 2006.
[20] Viswanathan, K., Shur, M. L., Spalart, P. R., and Strelets, M. K., "Computation of the Flow and Noise of Round and Beveled Nozzles," AIAA Paper 2006-2445, 2006.
[21] Bodony, D. J., Ryu, J., and Lele, S. K., "Investigating Broadband Shock-Associated Noise of Axisymmetric Jets Using Large-Eddy Simulation," AIAA Paper 2006-2495, 2006.
[22] Lo, S. C., Blaisdell, G. A., and Lyrintzis, A. S., "Numerical Simulation of Supersonic Jet Flows and their Noise," AIAA Paper 2008-2970, 2008.
[23] Imamoglu, B., and Balakumar, P., "Computation of Shock Induced Noise in Imperfectly Expanded Supersonic Jets," *International Journal of Aeroacoustics*, Vol. 6, No. 2, April 2007, pp. 127–146 (20). doi:10.1260/147547207781041877
[24] Berland, J., Bogey, C., and Bailly, C., "Numerical Study of Screech Generation in a Planar Supersonic Jet," *Physics of Fluids*, Vol. 19, No. 075105, 2007, pp. 1–14. doi:10.1063/1.2747225
[25] Grinstein, F. F., and Fureby, C., "On Monotonically Integrated Large Eddy Simulation of Turbulent Flows Based on FCT Algorithms," *Chapter 3 in Flux-Corrected Transport: Principles, Algorithms, and Applications*, edited by D. Kuzmin, R. Lohner, and S. Turek, Springer, New York, 2005, pp. 79–104.
[26] Lohner, R., "FEM-FCT: Combining Unstructured Grids with High Resolution," *Communications in Applied Numerical Methods*, Vol. 4, No. 6, 1988, pp. 717–729. doi:10.1002/cnm.1630040605
[27] Boris, J. P., and Book, D. L., "Flux-Corrected Transport I:SHASTA a Fluid Transport Algorithm That Works," *Journal of Computational Physics*, Vol. 11, No. 1, 1973, pp. 38–69. doi:10.1016/0021-9991(73)90147-2
[28] Kolbe, R. K., Kailasanath, K., Boris, J. P., and Young, T. R., "Numerical Simulation of Flow Modification of a Supersonic Rectangular Jets," *AIAA Journal*, Vol. 34, No. 5, May 1996.
[29] Boris, J. P., and Book, D. L., "Solution of Continuity Equations by the Method of Flux-Corrected Transport," *Controlled Fusion*, Academic Press, New York, 1976, pp. 85–129.
[30] Liu, J., Oran, E. S., and Kaplan, R., "Numerical Diffusion in the FCT Algorithm, Revisited," *Journal of Computational Physics*, Vol. 208, No. 2, 2005, pp. 416–434. doi:10.1016/j.jcp.2005.02.030
[31] Munday, D., Gutmark, E., Liu, J., and Kailasanath, K., "Flow and Acoustic Radiation from Realistic Tactical Jet C-D Nozzles," AIAA Paper 2008-2838, 2008.
[32] Prandtl, L., "Stationary Waves in a Gaseous Jet," *Physikalische Zeitschrift*, Vol. 4, No. 5, 1904, pp. 599–601.
[33] Norum, T. D., and Seiner, J. M., "Measurements of Mean Static Pressure and Far-Field Acoustics of Shock-Containing Supersonic Jets," NASA TM-84521, 1982.
[34] Tam, C. K. W., Seiner, J. M., and Yu, J. C., "Proposed Relationship Between Broadband Shock Associated Noise and Screech Tones," *Journal of Sound and Vibration*, Vol. 110, No. 2, 1986, pp. 309–321. doi:10.1016/S0022-460X(86)80212-7
[35] Seiner, J. M., Manning, J. C., and Ponton, M. K., "Model and Full Scale Study of Twin Supersonic Plume Resonance," AIAA Paper 87-244, 1987.

C. Bailly
Associate Editor